JACS
JOURNAL OF THE AMERICAN CHEMICAL SOCIETY

Article

[Cu32(PET)24H8Cl2](PPh4)2: A Copper Hydride Nanocluster with a Bisquare Antiprismatic Core

Sanghwa Lee, Megalamane S Bootharaju, Guocheng Deng, Sami Malola, Woonhyuk Baek, Hannu Häkkinen, Nanfeng Zheng, and Taeghwan Hyeon

J. Am. Chem. Soc., **Just Accepted Manuscript** • DOI: 10.1021/jacs.0c06577 • Publication Date (Web): 16 Jul 2020

Just Accepted

is published by the American Chemical Society. 1155 Sixteenth Street N.W., Washington, DC 20036

$[Cu_{32}(PET)_{24}H_8Cl_2](PPh_4)_2$: A Copper Hydride Nanocluster with a Bisquare Antiprismatic Core

Sanghwa Lee,[†,‡,⊥] Megalamane S. Bootharaju,[†,‡,⊥] Guocheng Deng,[§,⊥] Sami Malola,[∥] Woonhyuk Baek,[†,‡] Hannu Häkkinen,[*,∥] Nanfeng Zheng,[*,§] and Taeghwan Hyeon[*,†,‡]

[†]Center for Nanoparticle Research, Institute for Basic Science (IBS), Seoul 08826, Republic of Korea

[‡]School of Chemical and Biological Engineering, and Institute of Chemical Processes, Seoul National University, Seoul 08826, Republic of Korea

[§]State Key Laboratory for Physical Chemistry of Solid Surfaces, Collaborative Innovation Center of Chemistry for Energy Materials, and Department of Chemistry, College of Chemistry and Chemical Engineering, Xiamen University, Xiamen 361005, China

[∥]Departments of Physics and Chemistry, Nanoscience Center, University of Jyväskylä, FI-40014 Jyväskylä, Finland

ABSTRACT: Atomically precise coinage metal (Au, Ag and Cu) nanoclusters (NCs) have been the subject of immense interest for their intriguing structural, photophysical and catalytic properties. However, the synthesis of Cu NCs is highly challenging because of low reduction potential and high reactivity of copper, demonstrating the need for new synthetic methods using appropriate ligand combinations. By designing a diamine-assisted synthetic strategy, here we report the synthesis and total structure characterization of a box-like dianionic Cu NC, $[Cu_{32}(PET)_{24}H_8Cl_2](PPh_4)_2$ co-protected by 2-phenylethanethiolate (PET), hydride and chloride ligands. Its crystal structure comprises a rare bisquare antiprismatic $Cu_{14}H_8$ core, assembled by two square antiprisms by edge-sharing followed by hydride binding. The rod-shaped $Cu_{14}H_8$ core is clamped by two complex $Cu_7(PET)_{11}Cl$ and two simple Cu_2PET metal ligand frameworks, constructing the complete structure of Cu_{32} NC. The presence, number and location of hydrides are established by combined experimental and density functional theory results. The electronic structure calculations show the cluster as a zero-free-electron system, reproduce well the measured optical absorption spectrum and explain the main absorption features. Furthermore, the Cu_{32} cluster is found to be a highly active homogeneous catalyst for the C-N bond formation in aniline carbonylation reaction at room temperature. We hope that new findings in this work will stimulate and expand the research on Cu and other active metal NCs.

INTRODUCTION

The metal nanoclusters (NCs) or nanomolecules – systematically arranged few tens of metal atoms protected by a well-defined number of ligands – have been attracting great attention for both fundamental scientific studies and various potential applications.[1-4] The ultrasmall size (< 2 nm) and distinctly different atomic arrangement from their bulk counterparts impart metal NCs with unique molecular properties, including multiple absorption features, photoluminescence, isomerism, polymorphism and optical activity.[5-8] Unlike the average size and ill-defined composition of metal nanoparticles, the NCs are single-sized marked with precise chemical formulae, enabling the study of influence of size, structure, and electronic structure on the optoelectronic and catalytic properties.[9-12] Their remarkable characteristics, including high surface area, specific electronic interactions, photophysical properties, and intermediate stability between nanoparticles and bulk phase, make these NCs attractive for various applications such as chemical sensing, bio-imaging and catalysis.[13-18]

After the Brust-Schiffrin two-phase synthesis of small Au nanoparticles,[19] numerous thiolated Au and Ag NCs of different sizes and compositions have been synthesized.[1, 2, 20, 21] However, the research on the thiolated Cu NCs is lagging behind that of noble metal clusters largely due to high reactivity of Cu as well as low standard reduction potential for the half-cell reactions of $Cu(II/I) + ne^- \rightarrow Cu(0)$ (0.34 and 0.52 V, respectively; n is the number of electrons), preventing the systematic comparative studies of coinage metal NCs. In addition to thiolates, phosphines, halides, dithiocarbamates, sulfides, carboxylates, hydrides, alkynes or their combinations are potential ligands for Cu NCs.[3, 22-30] It has long been considered that the protecting ligands deactivate the catalytic activity of metal NCs as well as block the reactants from approaching metal sites.[13, 31] Partial or complete ligand removal is suggested for marking appreciable activity by compromising the size and structure of NCs. In particular, due to strong binding, the thiolates are anticipated to deactivate the Cu activity as compared to organometallic ligands such as hydrides and alkynes.[24] Consequently, more examples of solely thiolate or thiolate-rich Cu NCs are highly desirable to address the sulfur

poisoning in copper catalysis, which in turn requires new synthetic methods to overcome aforementioned challenges in the synthesis of Cu NCs.

The stabilizing ligands with appropriate degree of electronic effects direct the formation of metal NCs.[32] Of various thiolate ligands, 2-phenylethanethiolate (PET) has been most widely used to synthesize a wide-range of Au NCs, including Au_{20}, Au_{24}, Au_{25}, Au_{38}, Au_{40}, Au_{55}, Au_{67}, Au_{130}, Au_{137} and Au_{144}.[1] Therefore, it is very interesting to know the stable cluster size and the crystal structure that PET selects for under-explored Cu NCs. Given the synthetic challenges, we herein report on the diamine-assisted synthetic strategy to synthesize a Cu NC with the chemical formula $[Cu_{32}(PET)_{24}H_8Cl_2](PPh_4)_2$. Its crystal structure resolved by single crystal X-ray diffraction (SCXRD) reveals that the cluster has an unusual bisquare antiprismatic $Cu_{14}H_8$ core, which is further stabilized by two $Cu_7(PET)_{11}Cl$ and two Cu_2PET motifs. To the best of our knowledge, this core structure is observed for the first time in coinage metal NCs. The density functional theory is used to study the electronic structure and optical properties. Furthermore, we demonstrate that the Cu_{32} NC acts as an efficient homogenous catalyst for aniline carbonylation under mild reaction conditions.

RESULTS AND DISCUSSION

Synthesis, Purification and Crystallization. The synthesis of Cu_{32} NCs (**Scheme 1**) has two important steps. In the first step, a clear pale green solution of Cu(TMEDA)Cl complex (TMEDA: tetramethylethylenediamine) is obtained by reacting CuCl with TMEDA in tetrahydrofuran (THF) (**Figure S1** in Supporting Information). Subsequently, tetraphenylphosphonium bromide (PPh_4Br) and thiol (PETH) are added to the Cu(TMEDA)Cl complex, producing a yellowish CuPET(TMEDA)Cl turbid dispersion. In the second step, these metal ligand complexes are reduced with sodium borohydride ($NaBH_4$) to produce Cu NCs in an inert atmosphere (Ar). It is important to note that the use of both Cu source in +1 oxidation state and TMEDA is crucial for the formation of Cu_{32} NCs, where TMEDA assists the synthesis of Cu NCs despite being absent in the final product. The sources for hydride and chloride ligands in the cluster are $NaBH_4$ and CuCl, respectively. After completion of the reaction, the NC product is sequentially washed with ethanol and a mixture of THF and *n*-pentane to remove excess/unreacted reagents. Finally, a fully dried orange precipitate of Cu NCs is dissolved in a 1:1 (v/v) mixture of dichloromethane (DCM) and THF and the solution was layered with *n*-pentane at 5 °C, generating dark red single crystals (**Figure S2**) after a week (see Methods section for full details).

Scheme 1. Synthesis of $[Cu_{32}(PET)_{24}H_8Cl_2](PPh_4)_2$ NCs.

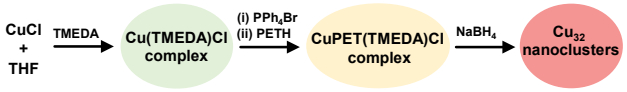

Crystal Structure and Mass Spectrometry. The SCXRD analysis of a suitable single crystal of the Cu cluster revealed that it consists of 32 Cu atoms and 24 PET and two Cl ligands. The unit cell of the cluster has two PPh_4^+ ions, indicating the electronic charge of the cluster is 2− (**Figures 1A** and **S3**). Although it is highly challenging to determine the hydrides through SCXRD due to low electron density of hydride, we were able to gain insights into the number and positions of the hydrides by careful SCXRD measurements, revealing a total of eight hydrides. Thus, the chemical formula for the cluster obtained from SCXRD is $[Cu_{32}(PET)_{24}H_8Cl_2](PPh_4)_2$. The presence of hydrides is also established by mass spectrometry and theoretical analysis, which are consistent with SCXRD results except a slight movement in two hydride positions (see DFT results, *vide infra*). The overall structure of the cluster has a box-like shape when viewed through crystallographic axes b (**Figure 1B**) and a (**Figure 1C**). The cluster crystallizes in a triclinic crystal system with *P-1* space group (**Table S1** in Supporting Information).

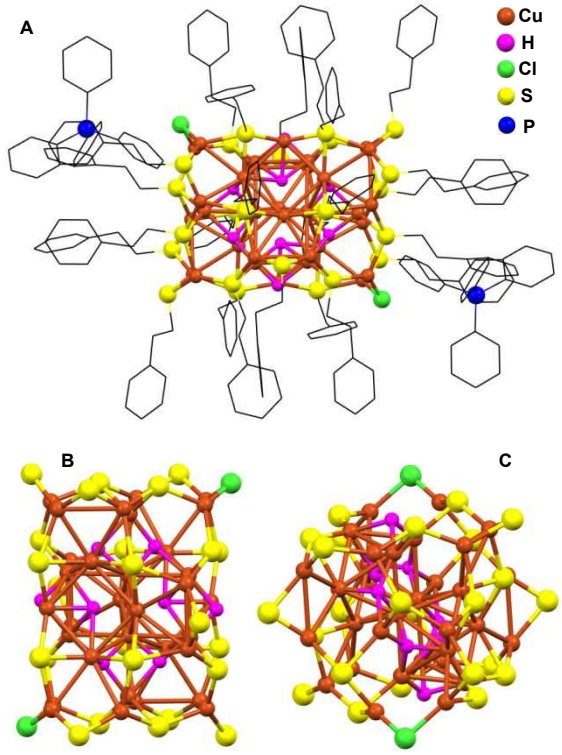

Figure 1. The crystal structure of $[Cu_{32}(PET)_{24}H_8Cl_2](PPh_4)_2$ NC. (A) Total structure showing two PPh_4^+ counterions. (B and C) Different views of the cluster down the crystallographic axes b and a, respectively. The carbon and phosphorous atoms of ligands and counterions are omitted in B and C for clarity.

A detailed structural analysis of the cluster (**Figure 2**) reveals that it has a core–shell structure with a $Cu_{14}H_8$ core and a $Cu_{18}(PET)_{24}Cl_2$ metal-ligand shell. Upon further inspection of the $Cu_{14}H_8$ unit, it is identified that two Cu_8 square antiprisms self-assemble into a rod-shaped Cu_{14} core by edge sharing (**Figure 2A**). Such a bisquare antiprismatic core is identified for the first time among coinage metal NCs, while icosahedral or cuboctahedral cores are common.[3, 22, 33] This Cu_{14} rod is further capped by eight hydrides, forming the full $Cu_{14}H_8$ core. Out of eight

hydrides, two of them are present inside two square antiprisms (**Figure 2A**) in μ-4 form (**Figure 2B**). The remaining six hydrides are located on six Cu_3 triangles of Cu_{14} unit (three each belong to one square antiprism) in μ-3 form. The metal ligand-shell of the cluster is made of two simple triangular Cu_2PET and two complex $Cu_7(PET)_{11}Cl$ motifs (**Figure 2B**). The $Cu_7(PET)_{11}Cl$ motifs appear as a crown, where both Cl are present in bridging (μ-2) mode. Notably, 22 PET ligands of the two large motifs appear in three types of bridging modes: 4 (μ-4), 12 (μ-3) and 6 (μ-2), where both thiolates in the Cu_2PET motifs are μ-2 type. The triangular Cu_2PET motifs are linked to the $Cu_{14}H_8$ rod on the opposite sides such that two Cu atoms in both motifs are parallel to the edge being shared by two square antiprisms. Finally, the two $Cu_7(PET)_{11}Cl$ motifs bind to the $Cu_{14}H_8$ core from its left and right side, generating the total structure of $Cu_{32}(PET)_{24}H_8Cl_2$ framework of the cluster (**Figure 2C**).

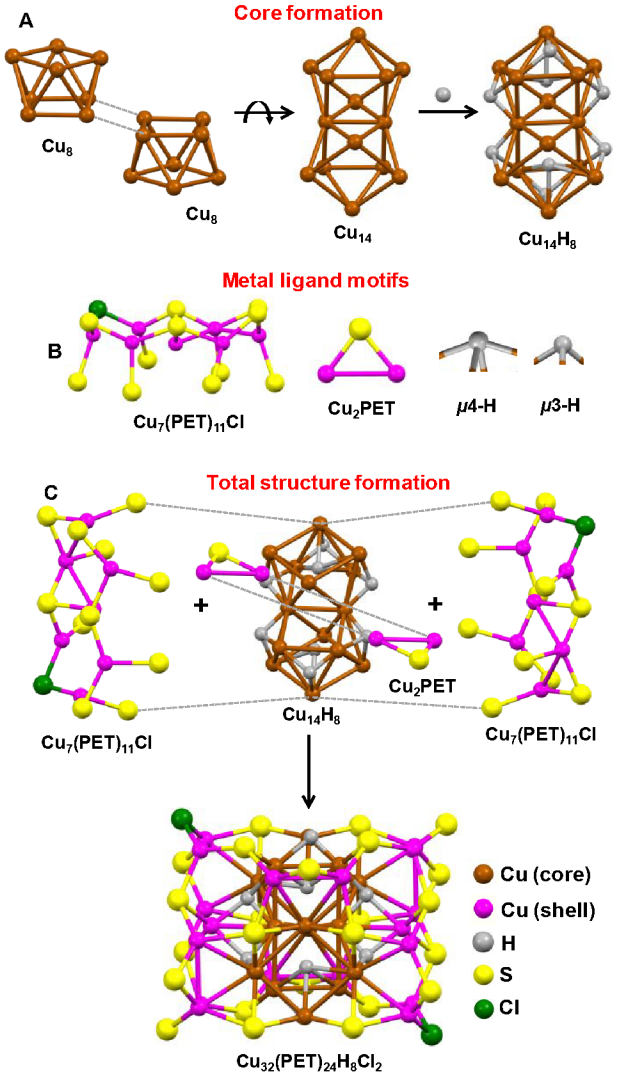

Figure 2. Analysis of the crystal structure of $[Cu_{32}(PET)_{24}H_8Cl_2](PPh_4)_2$ NC. (A) Formation of $Cu_{14}H_8$ core by edge sharing of two Cu_8 square antiprisms followed by capping with eight hydrides. (B) Metal ligand motifs of the cluster. (C) Linking of motifs with the $Cu_{14}H_8$ core, where each type of motifs approaches from opposite sides of the core. The carbon atoms of the ligands are not displayed for simplicity.

The Cu–Cu bond length in the $Cu_{14}H_8$ core is in the range of 2.537–2.785 Å, which is comparable to that in other copper clusters.[22, 26, 33, 34] Furthermore, the Cu_{core}–Cu_{shell} bond lengths range from 2.554 Å to 2.837 Å and the average value of Cu_{core}–Cu_{shell} bond lengths (2.720 Å) is higher than that within the $Cu_{14}H_8$ core (2.66 Å). In particular, the average Cu–Cu bond length (2.556 Å) in the Cu_6 plane, containing two edge shared Cu atoms and four Cu atoms from two square antiprisms, is very close to that of bulk Cu (2.556 Å),[35] indicating the strong interactions between two building blocks of Cu_{14} core. The Cu-S bond length ranges in $Cu_7(PET)_{11}Cl$ and Cu_2S motifs are 2.028-2.354 Å and 2.219-2.239 Å, respectively, while Cu-Cl bond length range is 2.131-2.184 Å.

The high resolution electrospray ionization mass spectrometry (HR-ESI-MS) is used to further characterize the composition and charge state of the cluster (**Figure S4**). The negative mode ESI-MS spectrum shows a high mass peak at m/z 2737 (**Figure 3A**, black trace). Upon expansion of this peak, several peaks with m/z 0.5 separation are observed, indicating that its charge state is 2−. By considering all the possible elements, the peak at m/z 2737 is assigned to a formula $[Cu_{32}(PET)_{24}H_6Cl_4]^{2-}$, consistent with the SCXRD result with respect to the number of Cu atoms and PET ligands as well as 2− charge state. This formula assignment is further validated by comparing the experimental spectrum with a simulated one, where both are found in very good agreement (**Figure 3B**), confirming that the Cu cluster has hydride ligands. Taking SCXRD and ESI-MS results together, we propose a formula of $[Cu_{32}(PET)_{24}H_8Cl_2]^{2-}$ for the as-synthesized Cu cluster. The $[Cu_{32}(PET)_{24}H_6Cl_4]^{2-}$ species in the mass spectrum may be originated by the gas phase atomic ligand exchange (two H with two Cl) between two Cu clusters, leading to other species $[Cu_{29}(PET)_{21}H_{10}]^{2-}$ and $[Cu_{28}(PET)_{20}H_{10}]^{2-}$ as well (**Figures 3A** and **S5**). This gas phase rearrangement of clusters can be represented as: $2[Cu_{32}(PET)_{24}H_8Cl_2]^{2-} \rightarrow [Cu_{32}(PET)_{24}H_6Cl_4]^{2-} + [Cu_{29}(PET)_{21}H_{10}]^{2-} + 3CuPET$. The replacement of only two H with two Cl is also supported by the crystal structure, where two hydrides are located close to surface, which can participate in such gas phase rearrangement (*vide infra*). The elemental analysis of the single crystals (**Figure S6**) further reveals that the original cluster has two Cl ligands, indicating that the $[Cu_{32}(PET)_{24}H_6Cl_4]^{2-}$ ion is produced in the gas phase. The $[Cu_{28}(PET)_{20}H_{10}]^{2-}$ is generated from $[Cu_{29}(PET)_{21}H_{10}]^{2-}$ by removing a CuPET unit. Note that our efforts to record a mass spectrum with the intact cluster feature for $[Cu_{32}(PET)_{24}H_8Cl_2]^{2-}$ were not successful by varying the experimental parameters of soft ionization. Such gas phase rearrangement of NC species in mass spectrometry conditions is not surprising as it is observed in other NCs when the ligand-shell comprises labile ligands.[34, 36]

To further confirm the presence of both hydrides and above characteristic fragmentation behavior of Cu_{32} cluster, a deuterated Cu cluster was synthesized by using $NaBD_4$ as the reducing agent in place of $NaBH_4$. Indeed, a mass spectrum with an upshift of m/z 3 from $[Cu_{32}(PET)_{24}H_6Cl_4]^{2-}$ i.e., a higher mass of 6 is observed (**Figure 3A**, blue trace). This upshifted peak corresponds to

a composition of $[Cu_{32}(PET)_{24}D_6Cl_4]^{2-}$, which is also verified by comparing its experimental spectrum with a calculated one (**Figure 3C**). More importantly, similar to $[Cu_{32}(PET)_{24}H_8Cl_2]^{2-}$ cluster, the $[Cu_{32}(PET)_{24}D_8Cl_2]^{2-}$ also shows gas phase atomic ligand exchange (D versus Cl), generating $[Cu_{32}(PET)_{24}D_6Cl_4]^{2-}$ and $[Cu_{29}(PET)_{21}D_{10}]^{2-}$ species (**Figure S5**), suggesting the unique behavior of Cu_{32} cluster under ESI conditions. These experimental results clearly suggest that the formula of the synthesized cluster is $[Cu_{32}(PET)_{24}H_8Cl_2]^{2-}$, which is also supported by free valence electron count rule, where this cluster has zero free electrons similar to other Cu NCs[22,28] (see also the following discussion on DFT results).

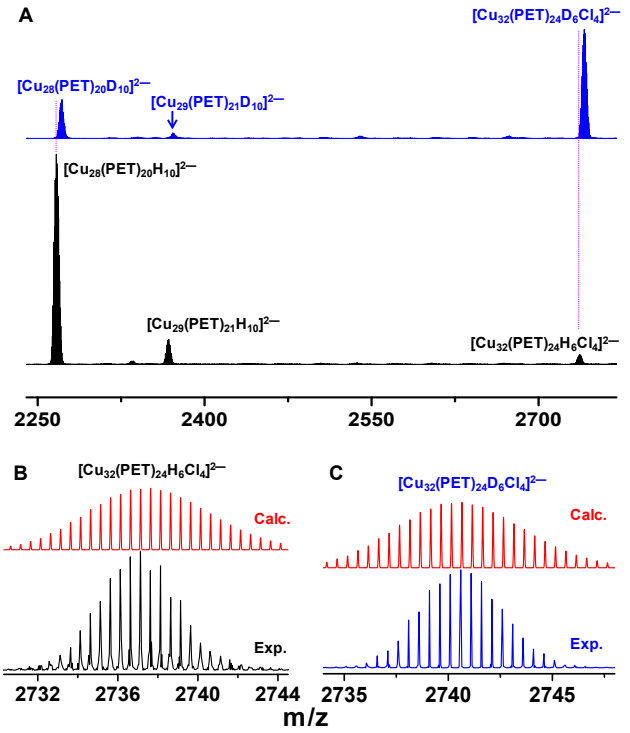

Figure 3. (A) HR-ESI-MS of $[Cu_{32}(PET)_{24}H_8Cl_2]^{2-}$ (black trace) and $[Cu_{32}(PET)_{24}D_8Cl_2]^{2-}$ (blue trace) NCs in negative ion mode. (B and C) Comparison of experimental mass spectra of the species $[Cu_{32}(PET)_{24}H_6Cl_4]^{2-}$ and $[Cu_{32}(PET)_{24}D_6Cl_4]^{2-}$ with their simulated ones, respectively. Exact match between them validates the composition assignment.

Modeling the Hydride Positions, Optical Properties and Cl → H Replacement by DFT. We performed extensive calculations of $[Cu_{32}(PET)_{24}H_8Cl_2]^{2-}$ using the density functional theory (DFT) in both its ground-state and time-dependent (TD-DFT) formalism (see technical details in the Methods in SI). We investigated the hydride positions in the copper core, the ground-state electronic structure, optical absorption, and replacement of hydrides with chlorines to yield the $[Cu_{32}(PET)_{24}H_6Cl_4]^{2-}$ cluster observed in the ESI-MS experiment.

We took the positions of copper atoms observed in the SCXRD experiment as a starting point and utilized our recently published algorithm[37] to propose the most probable positions for the hydrides in the system. A number of candidate structures proposed by the algorithm were then optimized with DFT computations. We observed that the algorithm consistently proposed hydride sites to positions where two chlorines were observed in the SCXRD data, additionally, two other hydride sites were close to the core-ligand interface, suggesting they might be amenable to Cl → H replacement reaction. The lowest-energy structures for the corresponding $[Cu_{32}(PET)_{24}H_8Cl_2]^{2-}$ and $[Cu_{32}(PET)_{24}H_6Cl_4]^{2-}$ clusters are shown in **Figure 4A** and **4B**, respectively. We observed that a model reaction $[Cu_{32}(PET)_{24}H_8Cl_2]^{2-} + Cl_2 \rightarrow [Cu_{32}(PET)_{24}H_6Cl_4]^{2-} + H_2$ is indeed *exothermic* by a gain of -1.55 eV yielding support for the interpretation of the ESI-MS data as discussed above. We also observed that a reaction to remove two chlorines and make the cluster with 10 hydrides would be highly *endothermic* by +3.99 eV.

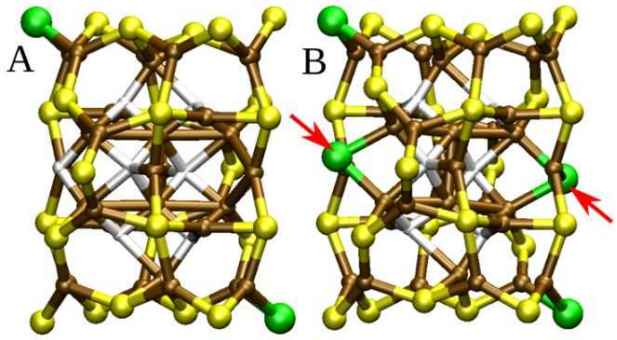

Figure 4. Optimal hydride sites in the core of (A) $[Cu_{32}(PET)_{24}H_8Cl_2]^{2-}$ and (B) $[Cu_{32}(PET)_{24}H_6Cl_4]^{2-}$ implied by the predictive algorithm[37]. The red arrows indicate the sites of the two extra Cl in (B).

The refined SCXRD data (**Figures 1** and **2**) and the predictive algorithm indicated six out of eight hydrides of $[Cu_{32}(PET)_{24}H_8Cl_2]^{2-}$ at identical sites, with the two remaining hydrides having 1.9 Å difference in position (**Figures S7** and **S8**). As a double check, we also started a DFT optimization from the experimental data but found out that these two hydrides moved to the sites predicted by the algorithm. While the reason for this discrepancy is unknown, we took the predicted optimal structure (**Figure 4A**) of the cluster as basis for all further analysis. The ground-state DFT calculation yields the electronic density of states as shown in **Figure 5**. The energy gap between the highest occupied (HOMO) and lowest unoccupied (LUMO) molecular orbitals is quite significant, 1.7 eV, which is in line with the experiment (**Figure S9**). Projection of the orbitals to spherical harmonics shows clearly that "superatom states" built from delocalized Cu electron states appear only in the unoccupied part of the spectrum, with a few states such LUMO to LUMO+3 having rather clear symmetries. This analysis confirms that there are no occupied delocalized free-electron states, *i.e.*, the cluster is not "metallic" but a zero-electron system.[38] Bader charge analysis (**Table S2**) confirms that the copper atoms are significantly positively and hydrogen atoms negatively charged, supporting the interpretation of formal H^- charge of hydrides in the copper core.

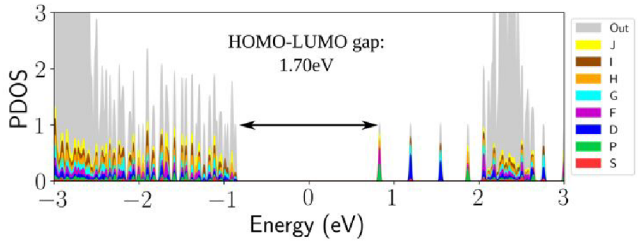

Figure 5. Projection of the Kohn-Sham molecular orbitals of $[Cu_{32}(PET)_{24}H_8Cl_2]^{2-}$ to spherical harmonics, with the HOMO-LUMO energy gap (1.7 eV) indicated.

The solution state UV-Vis absorption spectrum of $[Cu_{32}(PET)_{24}H_8Cl_2]^{2-}$ single crystals shows three features at 405, 460, and 550 nm labeled as A – C in **Figure 6**. The computed spectrum by using TD-DFT reproduces well the same features at 367, 447 and 552 nm (**Figure 6**). We analyzed the features A – C in the computed spectrum by using the so-called dipole transition contribution maps (DTCM). The analysis shown in **Figure S10** indicates that the lowest energy peaks at 552 and 447 nm consist of transitions from states within 1 eV below the HOMO to {LUMO, LUMO+2} states (mainly metal – metal transitions) while the peak at 367 nm has a considerable weight from metal-to-ligand transitions.

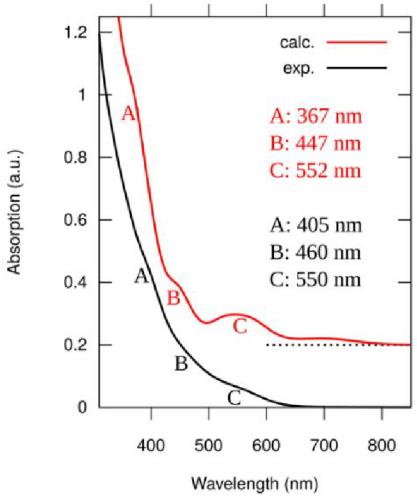

Figure 6. Experimental (black) and computed (red) UV-Vis absorption of $[Cu_{32}(PET)_{24}H_8Cl_2]^{2-}$. Three features A-C, identifiable in both spectra, are further analyzed in **Figure S10**.

Catalytic Activity. Several unique features of NCs, including the precise chemical formula and atomic structure, high monodispersity and intermediate stability, offer unprecedented opportunities to gain fundamental insights into the catalytic reactions.[13, 23, 29, 39, 40] The Cu based materials are known to be efficient homogenous catalysts for various organic reactions such as hydroboration, hydroamination, carbonylation and click reaction.[24, 41-43] Importantly, it is believed that sulfur poisons the Cu surface, leading to its no or low catalytic activity. But it is not yet fully understood about the catalytic activity of sulfur-bound Cu at the discrete atomic level due to the lack of thoroughly characterized Cu NCs.

We test the catalytic activity of $[Cu_{32}(PET)_{24}H_8Cl_2](PPh_4)_2$ NC towards a model reaction of carbonylation of anilines to produce carbamates through C-N bond formation (**Scheme 2**). We anticipate that amines such as anilines can have equilibrium interactions with clusters in solution because the Cu_{32} is synthesized using an assisting amine (TMEDA). Moreover, carbamates are an important class of chemicals used as herbicides, pharmaceuticals and starting materials in organic synthesis.[44, 45] Here, we perform the carbamate synthesis under mild conditions (at room temperature of 23 °C), contrast to the previous synthetic methods operating under harsh reaction conditions (high temperature) and using toxic CO gas as carbonyl source.[46] Specifically, Cu clusters in $CDCl_3$, aniline and methyl and halide substituted aniline are reacted with diisopropyl azodicarboxylate (DIAD) in an inert atmosphere for three hours (see Methods section for full details). Interestingly, the conversions for all the three anilines show 100%, indicating high catalytic activity of the thiolated Cu cluster. The isolated yields of the carbamate product, through column chromatography (**Figures S11-S13**), for aniline, methyl- and bromine-substituted aniline are found to be 60.5, 47.4 and 46.7%, respectively (**Table 1**). Furthermore, the NC catalyst can be reused without compromising the activity despite a slight reduction in the selectivity of the carbamate product.

Scheme 2. Carbonylation of Anilines.

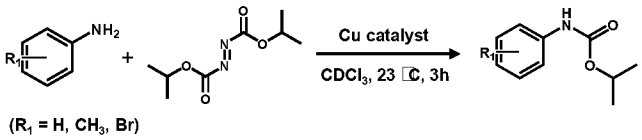

Table 1. Examples of C–N Bond Formation in Carbonylation of Anilines.

Catalyst	R_1	Product	Isolated Yield (%)
Cu_{32} NC	H	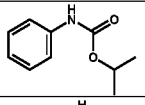	60.5
Cu_{32} NC	*p*-CH_3	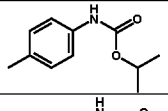	47.4
Cu_{32} NC	*p*-Br	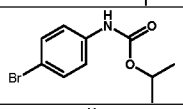	46.7
Cu_{32} NC	H	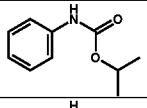	42.7[a]
CuPET thiolate	H	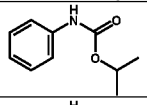	6.1
CuI salt	H	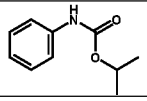	3.0

Reaction conditions: Cu_{32} cluster: 0.657 μmol; CuI: 21 μmol; CuPET thiolate: 20.9 μmol; anilines: 0.6 mmol; DIAD: 1.2 mmol; $CDCl_3$: 2 mL; temperature: 23 °C; time: 3 h. Conversion of anilines and purity of the carbamate product are obtained by ^{1}H NMR. [a]Isolated yield by reusing the Cu_{32} nanocatalyst after the first catalytic test.

Control experiments are performed, by replacing Cu_{32} clusters with a Cu salt (CuI) and CuPET thiolate complex for aniline carbonylation reaction under the same conditions, to identify the significance of Cu clusters in the catalysis. Surprisingly, CuI and CuPET show full aniline conversion; however, the desired carbamate product is insignificant (3.0 and 6.1%, respectively). The mechanism of aniline carbonylation is believed to proceed *via* formation of highly active oxyacyl radicals upon decomposition of DIAD on Cu catalyst. The specific interactions between aniline/aniline radicals and the surface of Cu_{32} would favor the formation of desired carbamate product (**Figure S14**). These interactions can be similar to those between TMEDA and Cu cluster during its synthesis. Due to lack of or minimized such specific interactions in the case of CuI or CuPET thiolate, aniline radicals would uncontrollably combine, resulting poor selectivity for carbamate product. Our catalytic results demonstrate that the thiolated Cu clusters can be not only active catalysts in homogeneous conditions even under mild conditions but also control the product selectivity *via* cluster surface-reactant interactions, contrast to the common belief of thiolate poisoning of Cu catalysis.

SUMMARY AND CONCLUSION

To summarize, a diamine assisted synthetic strategy is designed to synthesize a thiolate-rich Cu nanocluster. In the presence of an assisting TMEDA ligand, the thiolate, chloride and hydride ligands together form a Cu cluster with a chemical formula $[Cu_{32}(PET)_{24}H_8Cl_2]^{2-}$. Its X-ray crystal structure reveals an unprecedented bisquare antiprismatic $Cu_{14}H_8$ core shelled with $Cu_{18}(PET)_{24}Cl_2$ metal ligand framework. The composition of the cluster is confirmed by a series of control experiments using mass spectrometry. DFT not only supports the presence of hydrides but also identify their positions within the cluster, supporting the SCXRD results. TD-DFT is performed to understand the optical spectrum of the cluster. Furthermore, the Cu_{32} cluster is found to be a highly active homogeneous catalyst for carbamate synthesis through C-N bond formation in carbonylation of anilines. Our diamine assisted synthetic strategy may become a general method to synthesize NCs of other metals with novel crystal structures for various potential applications.

METHODS

Chemicals and Materials. All the chemicals used in our experiments are commercially available and are directly used without further purification. Cuprous chloride (CuCl, anhydrous, ≥99.99%), tetramethylethylenediamine (TMEDA, 99%), 2-phenylethanethiol (PETH, 98%), sodium borohydride ($NaBH_4$), sodium borodeuteride ($NaBD_4$, 98 atom% D), tetrahydrofuran (THF, anhydrous ≥99.9%), ethanol (anhydrous), *n*-pentane (anhydrous, ≥99%), deuterium oxide (D_2O, 99.9% atom D), dichloromethane (DCM), chloroform ($CHCl_3$, anhydrous ≥99%), aniline (ACS reagent, ≥99.5%), 4-bromoaniline (98%), diisopropyl azodicarboxylate (DIAD, 98%), ethyl acetate (EtOAc, 96%), hexane (99%) and deuterated chloroform ($CDCl_3$, 99.8%) were purchased from Sigma-Aldrich. Tetraphenylphosphonium bromide (PPh_4Br, 98%) and p–toluidine (98%) were received from Alfa Aesar.

Synthesis of $[Cu_{32}(PET)_{24}H_8Cl_2](PPh_4)_2$ Nanoclusters. All procedures for the synthesis of $[Cu_{32}(PET)_{24}H_8Cl_2](PPh_4)_2$ were performed under argon atmosphere using Schlenk techniques to avoid the oxidation of Cu source. To 20 mL of THF, 40 mg of CuCl and 60 μL of TMEDA were sequentially added. After vigorous magnetic stirring of the solution for 1 h, the reaction mixture turns clear pale green, forming Cu(TMEDA)Cl complex. To this, 40 mg of PPh_4Br in 0.5 mL methanol and 54 μL of PETH were added successively. The color of the solution turns from pale green to blue and turbid yellowish white immediately. After 30 minutes, $NaBH_4$ solution (80 mg $NaBH_4$ in 1 mL H_2O) was added dropwise to reduce metal ligand complexes to initiate the formation of nanoclusters. Upon continuous stirring for 1 h after $NaBH_4$ addition, the solution turns dark red, indicating the complete formation of nanoclusters. It is important to note that use of TMEDA and Cu (as Cu^+) is essential to synthesize this cluster. The crude product in THF was dried using a rotary evaporator and washed with ethanol once followed by multiple times with a *n*-pentane+THF mixture. Finally, an orange precipitate of Cu cluster was obtained and placed in a refrigerator (at 5 °C) for further use. For deuterated Cu_{32} clusters synthesis, above procedure is followed by replacing $NaBH_4$ in H_2O with $NaBD_4$ in D_2O.

Crystallization of $[Cu_{32}(PET)_{24}H_8Cl_2](PPh_4)_2$ Nanoclusters. The crystallization of the Cu cluster was conducted inside a glove box for better quality single crystals. About 20 mg of the purified cluster powder was dissolved in 2 mL of THF+DCM mixture (1:1 v:v) and the solution was filtered with a hydrophobic syringe filter. The filtrate was transferred to a 10 mL glass vial, layered with 3 mL of *n*-pentane and carefully stored inside a refrigerator (at 5 °C). After seven days, dark red single crystals of suitable quality were grown on the wall of the vial.

Catalytic Application of $[Cu_{32}(PET)_{24}H_8Cl_2](PPh_4)_2$ in Carbonylation of Anilines. The catalytic reaction of carbonylation of aniline and methyl and bromine substituted aniline was performed in a Ar filled glove box following a report with some modifications.[41] Typically, to the purified cluster powder (4 mg), 2 mL of $CDCl_3$, 55 μL of aniline (0.6 mmol) and 236 μL of DIAD (1.2 mmol) were sequentially added. The quantities of methyl and bromo anilines were 0.6 mmol and the other parameters unchanged. After stirring the reaction mixture for 3 h, the reaction was quenched with H_2O and the organic products were extracted with EtOAc. The EtOAc layer was separated and evaporated with a rotary evaporator. The organic products were purified by column chromatography using silica gel as the stationary phase and 5-10% (v/v) of ethyl acetate/hexane as the eluent. The conversion of anilines and the purity of the carbamate product were measured using ^{1}H NMR and the yield of the latter was calculated by weighing the isolated product. The turbid yellowish-white CuPET thiolate,

which is formed just before $NaBH_4$ addition in Cu_{32} cluster synthesis, was repeatedly washed with methanol and then used for catalysis for comparison.

ASSOCIATED CONTENT

Supporting Information. The Supporting Information is available free of charge at http://pubs.acs.org.

Synthesis, optical image of single crystal, ESI-MS, computational and catalytic property characterization of the $[Cu_{32}(PET)_{24}H_8Cl_2](PPh_4)_2$ cluster (pdf)

Crystallographic data for the $[Cu_{32}(PET)_{24}H_8Cl_2](PPh_4)_2$ cluster (CIF)

AUTHOR INFORMATION

Corresponding Authors

*thyeon@snu.ac.kr
*nfzheng@xmu.edu.cn
*hannu.j.hakkinen@jyu.fi

Author Contributions

⊥S.L., M.S.B. and G.D. contributed equally to this work.

Notes

The authors declare no competing financial interest.

ACKNOWLEDGMENTS

T.H. acknowledges the financial support by the Research Center Program of the IBS (IBS-R006-D1) in Korea. N.F.Z. acknowledges the financial support by the National Key Research and Development Program of China (2017YFA0207302), and the National Natural Science Foundation of China (21890752, 21731005, 21721001). The theoretical work at University of Jyväskylä was supported by the Academy of Finland (grants 292352 and 319208). The computations were done at the JYU node of the Finnish FGCI computing infrastructure.

REFERENCES

1) Jin, R.; Zeng, C.; Zhou, M.; Chen, Y. Atomically Precise Colloidal Metal Nanoclusters and Nanoparticles: Fundamentals and Opportunities. *Chem. Rev.* **2016**, *116*, 10346-10413.
2) Chakraborty, I.; Pradeep, T. Atomically Precise Clusters of Noble Metals: Emerging Link between Atoms and Nanoparticles. *Chem. Rev.* **2017**, *117*, 8208-8271.
3) Sharma, S.; Chakrahari, K. K.; Saillard, J. Y.; Liu, C. W. Structurally Precise Dichalcogenolate-Protected Copper and Silver Superatomic Nanoclusters and Their Alloys. *Acc. Chem. Res.* **2018**, *51*, 2475-2483.
4) Dhayal, R. S.; van Zyl, W. E.; Liu, C. W. Polyhydrido Copper Clusters: Synthetic Advances, Structural Diversity, and Nanocluster-to-Nanoparticle Conversion. *Acc. Chem. Res.* **2016**, *49*, 86-95.
5) Olaru, M.; Rychagova, E.; Ketkov, S.; Shynkarenko, Y.; Yakunin, S.; Kovalenko, M. V.; Yablonskiy, A.; Andreev, B.; Kleemiss, F.; Beckmann, J.; Vogt, M. A Small Cationic Organo–Copper Cluster as Thermally Robust Highly Photo- and Electroluminescent Material. *J. Am. Chem. Soc.* **2020**, *142*, 373-381.
6) Yoshida, H.; Ehara, M.; Priyakumar, U. D.; Kawai, T.; Nakashima, T. Enantioseparation and chiral induction in Ag_{29} nanoclusters with intrinsic chirality. *Chem. Sci.* **2020**, *11*, 2394-2400.
7) Chen, A.; Kang, X.; Jin, S.; Du, W.; Wang, S.; Zhu, M. Gram-Scale Preparation of Stable Hydride $M@Cu_{24}$ (M = Au/Cu) Nanoclusters. *J. Phys. Chem. Lett.* **2019**, *10*, 6124-6128.
8) Guan, Z.-J.; Hu, F.; Li, J.-J.; Wen, Z.-R.; Lin, Y.-M.; Wang, Q.-M. Isomerization in Alkynyl-Protected Gold Nanoclusters. *J. Am. Chem. Soc.* **2020**, *142*, 2995-3001.
9) Kang, X.; Abroshan, H.; Wang, S.; Zhu, M. Free Valence Electron Centralization Strategy for Preparing Ultrastable Nanoclusters and Their Catalytic Application. *Inorg. Chem.* **2019**, *58*, 11000-11009.
10) Bootharaju, M. S.; Chang, H.; Deng, G.; Malola, S.; Baek, W.; Häkkinen, H.; Zheng, N.; Hyeon, T. $Cd_{12}Ag_{32}(SePh)_{36}$: Non-Noble Metal Doped Silver Nanoclusters. *J. Am. Chem. Soc.* **2019**, *141*, 8422-8425.
11) Yang, D.; Pei, W.; Zhou, S.; Zhao, J.; Ding, W.; Zhu, Y. Controllable Conversion of CO_2 on Non-Metallic Gold Clusters. *Angew. Chem. Int. Ed.* **2020**, *59*, 1919-1924.
12) Kumar, B.; Kawawaki, T.; Shimizu, N.; Imai, Y.; Suzuki, D.; Hossain, S.; Nair, L. V.; Negishi, Y. Gold nanoclusters as electrocatalysts: size, ligands, heteroatom doping, and charge dependences. *Nanoscale* **2020**, *12*, 9969-9979.
13) Du, Y.; Sheng, H.; Astruc, D.; Zhu, M. Atomically Precise Noble Metal Nanoclusters as Efficient Catalysts: A Bridge between Structure and Properties. *Chem. Rev.* **2020**, *120*, 526-622.
14) Jiang, X.; Du, B.; Huang, Y.; Zheng, J. Ultrasmall noble metal nanoparticles: Breakthroughs and biomedical implications. *Nano Today* **2018**, *21*, 106-125.
15) Song, X.-R.; Goswami, N.; Yang, H.-H.; Xie, J. Functionalization of metal nanoclusters for biomedical applications. *Analyst* **2016**, *141*, 3126-3140.
16) Narouz, M. R.; Osten, K. M.; Unsworth, P. J.; Man, R. W. Y.; Salorinne, K.; Takano, S.; Tomihara, R.; Kaappa, S.; Malola, S.; Dinh, C.-T.; Padmos, J. D.; Ayoo, K.; Garrett, P. J.; Nambo, M.; Horton, J. H.; Sargent, E. H.; Häkkinen, H.; Tsukuda, T.; Crudden, C. M. N-heterocyclic carbene-functionalized magic-number gold nanoclusters. *Nat. Chem.* **2019**, *11*, 419-425.
17) Tang, Q.; Lee, Y.; Li, D.-Y.; Choi, W.; Liu, C. W.; Lee, D.; Jiang, D.-e. Lattice-Hydride Mechanism in Electrocatalytic CO_2 Reduction by Structurally Precise Copper-Hydride Nanoclusters. *J. Am. Chem. Soc.* **2017**, *139*, 9728-9736.
18) Shahsavari, S.; Hadian-Ghazvini, S.; Hooriabad Saboor, F.; Menbari Oskouie, I.; Hasany, M.; Simchi, A.; Rogach, A. L. Ligand functionalized copper nanoclusters for versatile applications in catalysis, sensing, bioimaging, and optoelectronics. *Mater. Chem. Front.* **2019**, *3*, 2326-2356.
19) Brust, M.; Walker, M.; Bethell, D.; Schiffrin, D. J.; Whyman, R. Synthesis of thiol-derivatised gold nanoparticles in a two-phase Liquid–Liquid system. *J. Chem. Soc., Chem. Commun*. **1994**, 801-802.
20) Gan, Z.; Xia, N.; Wu, Z. Discovery, Mechanism, and Application of Antigalvanic Reaction. *Acc. Chem. Res.* **2018**, *51*, 2774-2783.
21) Conn, B. E.; Atnagulov, A.; Yoon, B.; Barnett, R. N.; Landman, U.; Bigioni, T. P. Confirmation of a de novo structure prediction for an atomically precise monolayer-coated silver nanoparticle. *Sci. Adv.* **2016**, *2*, e1601609.
22) Nguyen, T. A. D.; Jones, Z. R.; Goldsmith, B. R.; Buratto, W. R.; Wu, G.; Scott, S. L.; Hayton, T. W. A Cu_{25} Nanocluster with Partial Cu(0) Character. *J. Am. Chem. Soc.* **2015**, *137*, 13319-13324.
23) Sun, C.; Mammen, N.; Kaappa, S.; Yuan, P.; Deng, G.; Zhao, C.; Yan, J.; Malola, S.; Honkala, K.; Häkkinen, H.; Teo, B. K.; Zheng, N. Atomically Precise, Thiolated Copper–Hydride

Nanoclusters as Single-Site Hydrogenation Catalysts for Ketones in Mild Conditions. *ACS Nano* **2019**, *13*, 5975-5986.
24) Cook, A. W.; Jones, Z. R.; Wu, G.; Scott, S. L.; Hayton, T. W. An Organometallic Cu_{20} Nanocluster: Synthesis, Characterization, Immobilization on Silica, and "Click" Chemistry. *J. Am. Chem. Soc.* **2018**, *140*, 394-400.
25) Baghdasaryan, A.; Besnard, C.; Lawson Daku, L. M.; Delgado, T.; Burgi, T. Thiolato Protected Copper Sulfide Cluster with the Tentative Composition $Cu_{74}S_{15}(2\text{-PET})_{45}$. *Inorg. Chem.* **2020**, *59*, 2200-2208.
26) Ghosh, A.; Huang, R. W.; Alamer, B.; Abou-Hamad, E.; Hedhili, M. N.; Mohammed, O. F.; Bakr, O. M. $[Cu_{61}(S^tBu)_{26}S_6Cl_6H_{14}]^+$: A Core–Shell Superatom Nanocluster with a Quasi-J_{36} Cu_{19} Core and an "18-Crown-6" Metal-Sulfide-like Stabilizing Belt. *ACS Mater. Lett.* **2019**, *1*, 297-302.
27) Ganguly, A.; Chakraborty, I.; Udayabhaskararao, T.; Pradeep, T. A copper cluster protected with phenylethanethiol. *J. Nanopart. Res.* **2013**, *15*, 1-7.
28) Li, J.; Ma, H. Z.; Reid, G. E.; Edwards, A. J.; Hong, Y.; White, J. M.; Mulder, R. J.; O'Hair, R. A. J. Synthesis and X-Ray Crystallographic Characterisation of Frustum-Shaped Ligated $[Cu_{18}H_{16}(DPPE)_6]^{2+}$ and $[Cu_{16}H_{14}(DPPA)_6]^{2+}$ Nanoclusters and Studies on Their H_2 Evolution Reactions. *Chem. Eur. J.* **2018**, *24*, 2070-2074.
29) Qu, M.; Zhang, F.-Q.; Wang, D.-H.; Li, H.; Hou, J.-J.; Zhang, X.-M. Observation of Non-FCC Copper in Alkynyl-Protected Cu_{53} Nanoclusters. *Angew. Chem. Int. Ed.* **2020**, *59*, 6507-6512.
30) Li, Y.-L.; Wang, J.; Luo, P.; Ma, X.-H.; Dong, X.-Y.; Wang, Z.-Y.; Du, C.-X.; Zang, S.-Q.; Mak, T. C. W. Cu_{14} Cluster with Partial Cu(0) Character: Difference in Electronic Structure from Isostructural Silver Analog. *Adv. Sci.* **2019**, *6*, 1900833.
31) Urushizaki, M.; Kitazawa, H.; Takano, S.; Takahata, R.; Yamazoe, S.; Tsukuda, T. Synthesis and Catalytic Application of Ag_{44} Clusters Supported on Mesoporous Carbon. *J. Phys. Chem. C* **2015**, *119*, 27483-27488.
32) Zeng, C.; Chen, Y.; Das, A.; Jin, R. Transformation Chemistry of Gold Nanoclusters: From One Stable Size to Another. *J. Phys. Chem. Lett.* **2015**, *6*, 2976-2986.
33) Chakrahari, K. K.; Silalahi, R. P. B.; Liao, J.-H.; Kahlal, S.; Liu, Y.-C.; Lee, J.-F.; Chiang, M.-H.; Saillard, J.-Y.; Liu, C. W. Synthesis and structural characterization of inverse-coordination clusters from a two-electron superatomic copper nanocluster. *Chem. Sci.* **2018**, *9*, 6785-6795.
34) Yuan, P.; Chen, R.; Zhang, X.; Chen, F.; Yan, J.; Sun, C.; Ou, D.; Peng, J.; Lin, S.; Tang, Z.; Teo, B. K.; Zheng, L.-S.; Zheng, N. Ether-Soluble Cu_{53} Nanoclusters as an Effective Precursor of High-Quality CuI Films for Optoelectronic Applications. *Angew. Chem. Int. Ed.* **2019**, *58*, 835-839.
35) Jaque, P.; Toro-Labbé, A. Characterization of copper clusters through the use of density functional theory reactivity descriptors. *J. Chem. Phys.* **2002**, *117*, 3208-3218.
36) Chai, J.; Yang, S.; Lv, Y.; Chen, T.; Wang, S.; Yu, H.; Zhu, M. A Unique Pair: Ag_{40} and Ag_{46} Nanoclusters with the Same Surface but Different Cores for Structure–Property Correlation. *J. Am. Chem. Soc.* **2018**, *140*, 15582-15585.
37) Malola, S.; Nieminen, P.; Pihlajamäki, A.; Hämäläinen, J.; Kärkkäinen, T.; Häkkinen, H. A method for structure prediction of metal-ligand interfaces of hybrid nanoparticles. *Nat. Commun.* **2019,** *10*, 3973.
38) Walter, M.; Akola, J.; Lopez-Acevedo, O.; Jadzinsky, P. D.; Calero, G.; Ackerson, C. J.; Whetten, R. L.; Grönbeck, H.; Häkkinen, H. A unified view of ligand-protected gold clusters as superatom complexes. *Proc. Natl. Acad. Sci.* **2008,** *105*, 9157-9162.
39) Du, X.; Jin, R. Atomically Precise Metal Nanoclusters for Catalysis. *ACS Nano* **2019**, *13*, 7383-7387.
40) Oliver-Messeguer, J.; Liu, L.; García-García, S.; Canós-Giménez, C.; Domínguez, I.; Gavara, R.; Doménech-Carbó, A.; Concepción, P.; Leyva-Pérez, A.; Corma, A. Stabilized Naked Sub-nanometric Cu Clusters within a Polymeric Film Catalyze C–N, C–C, C–O, C–S, and C–P Bond-Forming Reactions. *J. Am. Chem. Soc.* **2015**, *137*, 3894-3900.
41) Usman, M.; Ren, Z.-H.; Wang, Y.-Y.; Guan, Z.-H. Copper-catalyzed carbonylation of anilines by diisopropyl azodicarboxylate for the synthesis of carbamates. *RSC Adv.* **2016**, *6*, 107542-107546.
42) Xi, Y.; Hartwig, J. F., Mechanistic Studies of Copper-Catalyzed Asymmetric Hydroboration of Alkenes. *J. Am. Chem. Soc.* **2017**, *139*, 12758-12772.
43) Zhu, S.; Buchwald, S. L. Enantioselective CuH-Catalyzed Anti-Markovnikov Hydroamination of 1,1-Disubstituted Alkenes. *J. Am. Chem. Soc.* **2014**, *136*, 15913-15916.
44) Garcia Sanchez, F.; Cruces Blanco, C. Determination of the carbamate herbicide propham by synchronous derivative spectrofluorometry following fluorescamine-fluorogenic labeling. *Anal. Chem.* **1986**, *58*, 73-76.
45) Ghosh, A. K.; Brindisi, M. Organic Carbamates in Drug Design and Medicinal Chemistry. *J. Med. Chem.* **2015**, *58*, 2895-2940.
46) Guan, Z.-H.; Lei, H.; Chen, M.; Ren, Z.-H.; Bai, Y.; Wang, Y.-Y. Palladium-Catalyzed Carbonylation of Amines: Switchable Approaches to Carbamates and N,N′-Disubstituted Ureas. *Adv. Synth. Catal.* **2012**, *354*, 489-496.

Table of Contents